Turing patterns with pentagonal symmetry

J. L. Aragón

Instituto de Física, Universidad Nacional Autónoma de México, Apartado Postal 1-1010, Querétaro 76000, Mexico

M. Torres

Instituto de Física Aplicada, Consejo Superior de Investigaciones Científicas, Serrano 144, 28006 Madrid, Spain

D. Gil

Departamento de Paleontología, Facultad de Ciencias Geológicas, Universidad Complutense, Ciudad Universitaria, 28040 Madrid, Spain

R. A. Barrio

Instituto de Física, Universidad Nacional Autónoma de México, Apartado Postal 20-364, México 01000, Distrito Federal, Mexico

P. K. Maini

Centre for Mathematical Biology, Mathematical Institute, Oxford University, 24-29 St. Giles, Oxford OX1 3LB, United Kingdom

We explore numerically the formation of Turing patterns in a confined circular domain with small aspect ratio. Our results show that stable fivefold patterns are formed over a well defined range of disk sizes, offering a possible mechanism for inducing the fivefold symmetry observed in early development of regular echinoids. Using this pattern as a seed, more complex biological structures can be mimicked, such as the pigmentation pattern of sea urchins and the plate arrangements of the calyxes of primitive camerate crinoids.

PACS number(s): 87.10.+e, 71.23.An, 73.20.At

I. INTRODUCTION

The occurrence of pentagonally symmetric organisms has been largely surveyed and studied in detail [1,2]. For example, a pentagonal pattern is the basic pattern of the echinoderm skeletons. Some radiolarians and diatoms also provide notable examples of pentagonal patterns. However, most mathematical models for biological pattern formation exhibit hexagonal patterns [3–6] and the issue of selecting and stabilizing fivefold symmetric patterns has not been addressed in these models.

Motivated by the *de novo* appearance of pentagonal symmetry in the *rudiment disk* during the early development of regular echinoid larval forms (*echinopluteus*) [7], we carefully explore the formation of radially symmetric patterns using a Turing system solved on a confined circular domain with size comparable with the characteristic wavelength, starting from random initial conditions. Since under this aspect ratio the boundary controls the symmetry of the pattern, the radius of the disk (or the curvature of the circle) can be considered as the relevant parameter. Taking into account the wavelength of the Turing equations, we may expect a pentagonal pattern if system parameters and disk radius are adequately tuned, such that a central plus several marginal peaks are possible. We address this problem by studying numerically the Turing modes confined in a small size disk. As we shall show, the frustration induced by small disk radius reduces the usual hexagonal symmetry of the pattern, to produce pentagonally symmetric pattern. We also show that they are stable and, under large spatial homogeneities in the initial conditions, they appear over a well defined range of disk sizes. We also simulated numerically the situation when a

pentagonal seed is formed and used as a source of morphogen in a larger disk, as one might assume that in a biological system there is the possibility that a certain pattern (stable or not) can be frozen at a stage of development (calcified or biologically differentiated) and may serve as a seed for future development. These patterns compare notably well with the pigmentation pattern of *Toxopneustes pileolus* and, in a different context, still in the phylum of echinoderms, with the plate arrangements of the calyxes of primitive camerate crinoids [2]. All these results lead us to consider morphogenesis as a step by step process in the sense that once a pattern is generated and biologically consolidated, it can serve as a seed for the next step. It also reinforces the importance of transient or unstable patterns in biological systems [8].

II. THE MODEL

In all biological models there remain uncertainties about the mechanisms behind pattern formation: the study of genetics alone cannot provide us with such mechanisms. Perhaps the most extensively studied mechanism for self-organized biological pattern formation is the Turing instability [9–11] and we focus our attention on this mechanism. Albeit the molecular details are still unknown, the Turing model has been shown to exhibit pigment patterns consistent with those observed in some mammals [12], seashells [13], and marine fishes [14–18]. Curved geometries have also been introduced to model microscopic organisms such as radiolarians [19] and patterns on the hard wings of lady beetles [20]. Recently, it has been found that morphogens (the name given by Turing to the chemicals in prepattern models) do exist [21], but experimental evidence that mor-

phogen patterns are set up by a Turing mechanism is yet to be found.

Turing equations describe the temporal development of the concentrations of two chemicals, U and V, that diffuse at different rates, D_U and D_V, and react according to the non-linear functions f and g,

$$\frac{\partial U}{\partial t} = D_U \nabla^2 U + f(U,V),$$

$$\frac{\partial V}{\partial t} = D_V \nabla^2 V + g(U,V).$$

We take the model introduced by Barrio *et al.* [17], obtained by observing that, in general, there is a stationary uniform solution (U_c, V_c), given by the zeros of f and g. Functions are then expanded around this point in a Taylor series, neglecting terms of order higher than cubic. The specific system we consider is

$$\frac{\partial u}{\partial t} = D\delta\nabla^2 u + \alpha u(1 - r_1 v^2) + v(1 - r_2 u), \quad (1a)$$

$$\frac{\partial v}{\partial t} = \delta\nabla^2 v + \beta v\left(1 + \frac{\alpha r_1}{\beta} uv\right) + u(\gamma + r_2 v), \quad (1b)$$

where $u = U - U_c$, $v = V - V_c$, $D_U = D$, and $D_V = 1$. The quantity δ conveniently gives the size of the system, and the particular arrangement of the coefficients obeys conservation rules in these chemicals. There are two interaction parameters r_1 and r_2 that, in Cartesian coordinates, control the formation of stripe or spot patterns, respectively [17].

We investigate patterns in a two-dimensional disk with zero-flux boundary conditions, namely,

$$\mathbf{n} \cdot \boldsymbol{\nabla} u(r,\theta) = \mathbf{n} \cdot \boldsymbol{\nabla} v(r,\theta) = 0,$$

for all $\theta \in [0, 2\pi)$, with r at the boundary of the disk with unit outward normal $\mathbf{n}$. We then, in the linear regime, look for solutions of the form (in the usual way)

$$u = u_0 \exp(\lambda t) \sum_m C_m J_m(kr)\exp(im\theta),$$

$$v = v_0 \exp(\lambda t) \sum_m D_m J_m(kr)\exp(im\theta),$$

where C_m and D_m are constants and J_m are Bessel functions of mth order of the first kind. By substituting these solutions in the linearized version of Eq. (1) we obtain that the dispersion relation is given by the solutions of

$$\lambda^2 + [(1+D)\delta\kappa^2 - \beta - \alpha]\lambda + [(D\delta\kappa^2 - D\beta - \alpha)\delta\kappa^2$$
$$+ \alpha(\beta+1)] = 0. \quad (2)$$

In order to keep the solutions as simple as possible, we enforced $(0,0)$ to be the only spatially uniform steady state by setting $\alpha = -\gamma$ [17]. The following conditions must be satisfied for diffusion-driven instability [10,17]:
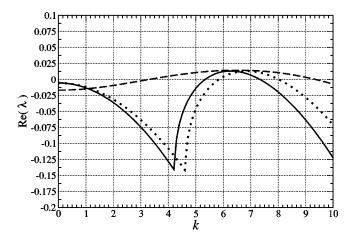

FIG. 1. Variation of dispersion relation, from Eq. (2), for different parameter values. The continuous line corresponds to $\alpha = 0.899$, $\beta = -0.91$, $D = 0.516$, and $\delta = 0.01011$, to enhance the mode $k_{51} = 6.41562$. The dotted line corresponds to the same parameters as in the previous case but with $\delta = 0.00845$ to enhance the mode $k_{03} = 7.01558$. Finally, the dashed line corresponds to the same mode k_{03}, but obtained with parameter values $\alpha = 0.2334$, $\beta = -0.95$, $D = 0.12$, and $\delta = 0.01011$.

$$f_U + g_V < 0 \Rightarrow \alpha + \beta < 0,$$

$$f_U g_V - f_V g_U > 0 \Rightarrow \alpha(\beta + 1) > 0,$$

$$D_U g_V + D_V f_U > 0 \Rightarrow \delta(D\beta + \alpha) > 0,$$

$$(D_U g_V + D_V f_U)^2 - 4D_U D_V(f_U g_V - f_V g_U) > 0$$
$$\Rightarrow (D\beta + \alpha)^2 - 4D\alpha(\beta+1) > 0, \quad (3)$$

where subscripts in f and g denote differentiation.

At the onset of instability, a good approximation of the critical wave vector is given by the minimum of the left part of the last inequality in Eq. (3), namely,

$$k_c^2 = \frac{D_V f_U + D_U g_V}{2D_U D_V} = \frac{1}{\delta}\left(\frac{\alpha + D\beta}{2D}\right), \quad (4)$$

where $k = k_{mn} = \kappa_{mn} a$; κ_{mn} is the nth zero of the derivative of the Bessel function J'_m and a is the radius of the disk. Observe that this equation implies that once (a, α, β, D) are fixed, one could select a pattern of a given radial symmetry by varying δ. Alternatively, solving Eq. (4) for δ, one could tune the other parameters to satisfy the condition $k = \kappa_{mn}/a$ for a given symmetry m.

In Fig. 1 we show the dispersion relation, from Eq. (2), for a selection of different parameter values in the appropriate parameter domain defined by Eq. (3). The parameters were chosen to enhance mode $k_{51} = \kappa_{51} = 6.41562$ (in what follows, we shall consider a unitary disk, $a = 1$), according to Eq. (4), and mode $k_{03} = \kappa_{03} = 7.01558$ was enhanced using two different sets of parameter values.
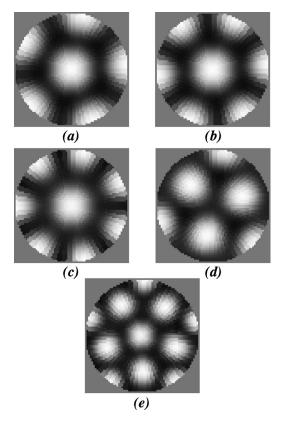
(a)   *(b)*

(c)   *(d)*

(e)

FIG. 2. Series of symmetries obtained in a disk with zero-flux boundary conditions. The values of δ are (a) 0.01 011, (b) 0.0075, (c) 0.0055, (d) 0.0065, and (e) 0.0037. These correspond to selecting modes k_{51}, k_{61}, k_{71}, k_{32}, and k_{52}, respectively.
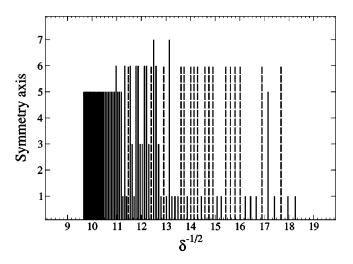

FIG. 3. Value of the pattern symmetry axis versus $\delta^{-1/2}$, which is proportional to the radius of the disk, for simulations with parameter values $\alpha = 0.899$, $\beta = -0.91$, $D = 0.516$, $a = 1$, and $r_1 = r_2 = 0.2$. The dashed lines represent noncentrosymmetric sixfold patterns. Onefold symmetry axis corresponds to mixed symmetries. Below $\delta^{-1/2} = 9.66$, noncentrosymmetric patterns with four or less spots are obtained and for $\delta^{-1/2} > 18.25$ hexagonal patterns with defects are generated. Starting from $\delta = 0.001$ ($\delta^{-1/2} = 31.623$) patterns were obtained by increasing δ by 0.0001 and, in each case, we used 36×10^6 time iterations to converge, with a time step of $\Delta t = 1 \times 10^{-4}$.

III. NUMERICALLY COMPUTED STEADY-STATE PATTERNS

Equations (1) are solved in polar coordinates in a unitary disk ($a = 1$) by a simple Euler method as described in detail in Appendix A. The calculations reported here were carried out using grid parameters $M = 34$, $N = 68$, $\Delta r = 1/34$, and $\Delta \theta = 2\pi/68$. The parameter values (kept fixed in all our simulations) are $\alpha = 0.899$, $\beta = -0.91$, and $D = 0.516$. We used 16×10^6 time iterations to converge, with a time step of $\Delta t = 1 \times 10^{-4}$, which fulfills the necessary condition for numerical stability (A9). The system was always initialized using random fluctuations (± 0.5) around the steady state $U_{i,j}^0 = 0$ and $V_{i,j}^0 = 0$, for all i,j. The seed of the random generator was set to the CPU time of the computer.

In Fig. 2, examples of patterns obtained with parameter values $r_1 = r_2 = 0.2$, to produce a spot pattern [17], are shown. The values of δ correspond to increasing the size of the domain and, according to Eq. (4), different symmetries are selected. The convergence to steady state of the pattern was estimated by means of the quantity $\sigma = \Sigma_{i,j}(U_{i,j}^n - U_{i,j}^{n-1})^2$, at each time step. A typical value of this quantity in all our calculations is 1×10^{-6}. In Fig. 3 a graph of the pattern symmetry axis value versus δ is shown. It can be seen that hexagonal and pentagonal patterns are more frequent and the pentagonal pattern is generated in a range of δ about 16% of the explored radius. The use of the circular

geometry to solve the Turing equations allows us to generate a fivefold pattern.

The appearance of the central spot in some of the patterns in Fig. 2 may seem strange at first sight. In particular, $J_5(k_{51}r)$ is zero at the origin and Fig. 2(a) shows nonzero values there. We should, however, note that the linear analysis predicts modes under the linear regime, while the final solution depends also on the nonlinear terms and it is expected that, besides monomodes, nonlinear coupling of different modes may appear. In Appendix B we perform a modal decomposition of a pentagonal pattern to confirm this possibility.

Since in Appendix A we obtain only necessary conditions for numerical stability, we performed a number of simulations with different step sizes (in time and space) in order to verify that the solution does not change under these conditions. In Figs. 4(a) and 4(b), we show the pentagonal pattern obtained with the same parameters as in Fig. 2(a) but with smaller time steps, namely, 5×10^{-5} and 1×10^{-5}, respectively. In Fig. 4(c) we changed the spatial step size to $M = N = 68$, with $\Delta t = 2 \times 10^{-5}$. Finally, in Fig. 4(d), a plot of the convergence factor σ for the simulations in Figs. 4(a) and 4(b) is shown.

In the range of disk sizes where we obtain pentagonally symmetric solutions, other admissible modes are possible and we found that under several different runs, with different initial conditions, it was possible to obtain these modes (but only if we reduce the amplitude of the random fluctuations in the initial conditions). This problem of multiple stable steady-state solutions has been one of the main criticisms of the Turing model as a plausible explanation for robust pattern formation. It has been shown that using different types of boundary conditions [22] or employing domain growth
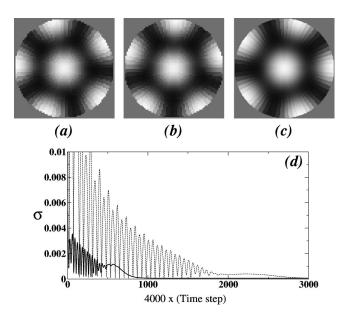
FIG. 4. Simulations of the pentagonal pattern with the same parameters as in Fig. 2(a) but with different spatial and temporal step sizes. (a) $\Delta t = 5 \times 10^{-5}$, (b) 1×10^{-5}, (c) $M = N = 68$, and $\Delta t = 2 \times 10^{-5}$, and (d) plot of the convergence factor σ for the simulations in (a), with continuous line, and (b) with dashed line.

[23] it is possible (at least on a one-dimensional domain) to increase greatly the robustness of certain modes.

IV. PATTERNS OF SEA URCHINS

Selecting the symmetry of the Turing pattern by means of the disk radius may be relevant for capturing the essence of the *de novo* appearance of the five primary podia during the early development of regular echinoid larval forms. At the first stages of larval growth, these animals develop five buds of primary podia in a disk called *imaginal rudiment*, *rudiment disk*, or just *rudiment* [7,24,25]. These five buds point to the vertices of a slightly distorted pentagon and give rise to the radially symmetric adult. In Figs. 5(a) and 5(b), schematic diagrams of the realistic arrangement of the five primary podia in the rudiment of *Eucidaris thouarsi* and *Strongylocentrotus droebachiensis* sea urchin larvae are
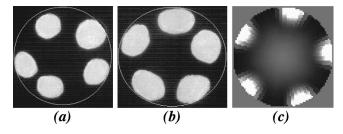

FIG. 5. Schematic diagrams showing the realistic arrangement of the five primary podia in the rudiment of (a) *Eucidaris thouarsi* larvae (taken from Fig. 2 of Ref. [7]) and (b) *Strongylocentrotus droebachiensis* sea urchin larvae [taken from Fig. 2(f) of Ref. [25]]. (c) Numerical calculation of the pentagonal pattern with the same parameters as in Fig. 2(a) but with the factors that control the formation of stripes or spots changed to $r_1 = 5$ and $r_2 = 3$.

shown [26]. Much of the rest of larval growth consists of the formation and lengthening of podial buds maintaining the pentagonal symmetry of the initial lobes. These five podial buds play a major role, by migration from pole to pole, during the embryological skeletal development of regular echinoids in the framework of the axial-extraxial theory [27]. Thus, the symmetry of the adult echinoid is set in this initial stage of development and, for this purpose, the first relevant event is the formation of a pentagonal pattern in the rudiment that dictates the radial symmetry of future development.

Regarding ratios and relative sizes, the realistic diagrams in Figs. 5(a) and 5(b) compare notably well with Fig. 2(a) with the exception of the central spot in the latter. In Fig. 5(c) we show a simulation with the same parameters as in Fig. 2(a) but the factors that control the formation of stripes or spots were changed to $r_1 = 5$ and $r_2 = 3$. Generally, spots are more robust and pronounced than stripes [17]; actually, stripes are only formed for very small values of r_2. In the simulation of Fig. 5(c), the factor favoring stripes is high, they do not form because r_2 is not small. The net result is a sort of modulation of amplitudes such that the central spot of the pentagon, albeit present, has a very low amplitude.

Notice that taking into account how the symmetry of the patterns are selected, from a genetic point of view, the pentagonal symmetry of the adult echinoid can be efficiently encoded using two basic parameters as highly condensed instructions: the radius of the rudiment disk (or the cell number) and the characteristic wavelength of the morphogens.

Let us now consider the case when a given pattern is used as source of morphogens in a larger disk. That is, we simulate the influence of an initially frozen pattern in a domain where a pattern forming reaction takes place. This has been used to simulate the imposition of some directional preference onto the pattern formed, by means of a pattern of differentiated cells [28–30]. We first consider the pentagonal structure shown in Fig. 2(a) implanted as a source of morphogens in a disk of larger size. The procedure is as follows. The spots of the pentagonal structure shown in Fig. 2(a), generated in a disk of radius r (proportional to $1/\sqrt{\delta_r}$, with $\delta_r = 0.01\,011$), is implanted in a larger disk of radius $R > r$ (proportional to $1/\sqrt{\delta_R}$, with $\delta_R = 0.0006$), and its amplitude scaled such that the maximum equals 1. The system is then initialized with the previous pentagonal pattern as a seed at the center and $U_{i,j}^0 = V_{i,j}^0 = 0$ in the area not occupied by the spots of the pentagonal seed. These spots are considered a source of morphogen in such a way that their size is maintained fixed and the value of the morphogen is set to 1 during all time steps. In Fig. 6(a) we show the pattern that results after 800 000 iterations (before reaching steady state). The pattern compares notably well with the pigmentation pattern of the common Indo-Pacific sea urchin species *Toxopneustes pileolus* (Alphonso urchin), shown in Fig. 6(b), and it may be considered as a frozen pattern when the animal reaches adulthood. The similarities between the simulated pattern and the real biological pattern are supported by the coherence between the pigmentation pattern and the morphological structure of the urchin test [as seen in Fig. 6(b)], suggesting that both pigmentation and skeleton formation were simultaneous during the growth process.
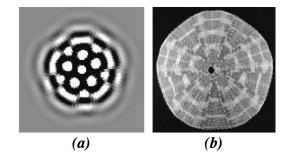
FIG. 6. (a) Transient pattern (after 800 000) iterations obtained with $\delta=0.0006$ using a pentagonal seed as described in the text with the remaining parameter values as in Fig. 2. (b) *Toxopneustes pileolus* sea urchin (taken from echinoid website of The Natural History Museum of London, designed by A. Smith).

V. PATTERNS OF CRINOIDS

In a second simulation we let the pattern of Fig. 6(a) reach stability (6×10^6 time iterations). The final pattern is shown in Fig. 8(a) and it consists of a nearly twinned pentagonal structure. The disk size used in the simulation ($\delta_R=0.0006$) is large enough to obtain a hexagonal pattern, but in this case it has to couple with the pentagonal seed and the best way to do this is to generate a twinned structure formed by a central pentagon surrounded by distorted hexagons.

This result can be related to another important and primitive taxonomic group of echinoderms: the crinoids [31]. In Fig. 7 we show the typical plate diagrams of 11 calyxes of camerate crinoid fossils that we have studied [2,32]. An interesting fact is that all these structures are variations of a fundamental arrangement that is a twinned pentagonal structure. This can be made evident as follows. By using the numerical approach described elsewhere [2], we digitalize each plate diagram codifying the result using a binary system: black (1) and the white background (0). Next, we expand this binary function as a truncated Fourier-Bessel series with real coefficients [2] so that a plate arrangement can be described by the plate model function

$$T(r,\theta)=\sum_{n=0}^{4}J_{5n}(kr)[C_{5n}\cos(5n\theta)+S_{5n}\sin(5n\theta)],$$
(5)

where r and θ are polar coordinates and k is the wave number [2]. The values of C and S were calculated for the 11 fossil species shown in Fig. 7 and it turns out that all structures are quite similar [2]. An average structure can be obtained by taking the mean of the calculated constants C and S of the 11 species studied, giving $C_0=0.25$, $C_5=0.05$, $C_{10}=-0.45$, $C_{15}=0.02$, $C_{20}=0.48$, $S_5=0.47$, $S_{10}=-0.02$, $S_{15}=-0.46$, and $S_{20}=0.05$. Notably, this undulatory average structure is an almost perfect fivefold twinned structure, as shown in Fig. 8(c), which compares well with the twinned Turing structure that results from our simulation, and is shown in Fig. 8(a).

In order to compare both patterns in a more proper way, the simulated structure of Fig. 8(a) was transformed to a black and white image and the Fourier-Bessel analysis gives
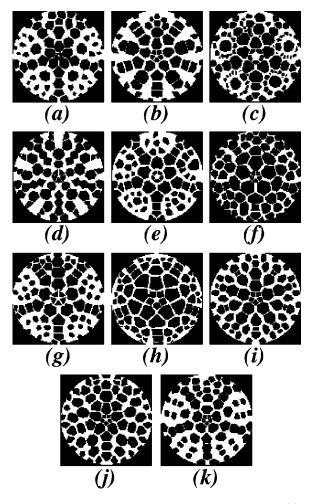

FIG. 7. Typical plate diagrams of camerate crinoids: (a) *Archaeocrinus microbasalis*, (b) *Condylocrinus verrucosus*, (c) *Deocrinus asperatus*, (d) *Diamenocrinus jouani*, (e) *Hercocrinus elegans*, (f) *Kyreocrinus constellatus*, (g) *Opsiocrinus mariana*, (h) *Ortsaecrinus cocae*, (i) *Rhodocrinites kirbyi*, (j) *Sphaerotocrinus ornatus*, and (k) *Thylacocrinus vannioti*.

$C_0=0.25$, $C_5=0.09$, $C_{10}=-0.42$, $C_{15}=-0.04$, $C_{20}=0.45$, $S_5=0.36$, $S_{10}=-0.1$, $S_{15}=-0.28$, and $S_{20}=0.26$, which compare well with the averaged coefficients of the fossil species. This good match is better appreciated if we reproduce the image using these coefficients and Eq. (5). The resulting
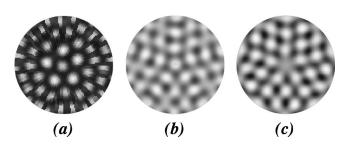

FIG. 8. (a) Final steady-state pattern of the simulation shown in Fig. 6(a) after 6×10^6 time iterations. (b) Pattern obtained using Eq. (5) and the coefficients of the Fourier-Bessel analysis of (a). (c) Average twinned structure of the arrangement of plates of camerate crinoids.
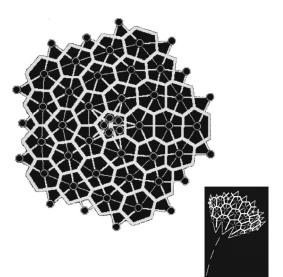
FIG. 9. Schematic plate arrangement of *Pycnocrinus dyeri* fossil crinoid. Plates are indicated by thick white lines. Circles indicate the center of the plates and form a lattice of ridges decorating the plates. This lattice (drawn with thin white lines) is a twinned pentagonal structure formed by distorted hexagons with a pentagon at the center. The inset shows a schematic diagram of the calyx or cup of *Pycnocrinus dyeri* adult form from where the plate diagram was obtained.

pattern is shown in Fig. 8(b). Both undulatory patterns (averaged and mimicked) are pentagonal twinned structures with the property that the sides of the central pentagon are also sides of antinode hexagons surrounding this pentagon.

Our Turing model thus captures the essence of these structures that evolution has explored in crinoids, which are fluctuations of a basic pentagonal twinned structure. This average structure is a simple and predictable geometrical pattern that evolution may have occupied in the morphospace of early crinoid skeletons. Hence, this is another example that corroborates the claim of the more general work by Thomas *et al.* [33], where it is established that viable design elements available for animals, to use as skeletons, have been fully exploited in early ages. Evidently, evolution also tried the twinned structure itself, as can be seen in Fig. 9, where the schematic plate arrangement of *Pycnocrinus dyeri* camerate crinoid fossil [31,32] is shown. In the figure, plates are indicated by thick white lines. The centers of the plates are indicated by circles and form a lattice of ridges decorating the plates. Observe that this lattice (drawn with thin white lines) is a twinned pentagonal structure formed by distorted hexagons with a pentagon at the center, quite similar to the ones shown in Fig. 8. Notice also that plates constitute the Dirichlet domains of the lattice of ridges [34]. This plate arrangement is also observed in *Glyptocrinus decadactylus* camerate crinoid fossil [31,32].

The plate arrangement shown in Fig. 9 was directly obtained from the calyx or cup of the published images of fossil crinoids [31,32]. A schematic diagram of the calyx is shown in the inset of Fig. 9; the stem of the fossil is represented by the three white lines at the bottom of the figure and white filled circles indicate the starting point of the arms.

VI. CONCLUSIONS

We have explored numerically the formation of Turing patterns in a circular domain with size comparable with the characteristic wavelength. Our results show that, under large spatial homogeneities in the initial random conditions, pentagonal patterns appear and are stable over a well defined range of disk sizes (about 16% of the explored radius). Some real biological examples of pentagonal patterns in regular echinoids and criuoids are presented. Our results may offer a possible mechanism for inducing the fivefold symmetry observed in early development of these animals. By assuming that in a biological system a certain pattern can be calcified or biologically differentiated at a stage of development, we also simulate pigmentation patterns in sea urchin shells by using sources of morphogens implanted in a disk. Finally, the importance of a transient or an unstable pattern in biological systems is reinforced.

APPENDIX A: FINITE-DIFFERENCE SCHEME

By using subscripts to denote differentiation, in polar coordinates the Laplacian reads

$$\nabla^2 = \partial_{rr} + \frac{1}{r^2}\partial_{\theta\theta} + \frac{1}{r}\partial_r .$$

The system (1) is then

$$u_t = D\delta\left(u_{rr} + \frac{1}{r^2}u_{\theta\theta} + \frac{1}{r}u_r\right) + \alpha u(1 - r_1 v^2) + v(1 - r_2 u),$$
(A1a)

$$v_t = \delta\left(v_{rr} + \frac{1}{r^2}v_{\theta\theta} + \frac{1}{r}v_r\right) + \beta v\left(1 + \frac{\alpha r_1}{\beta}uv\right) + u(\gamma + r_2 v),$$
(A1b)

with zero-flux boundary conditions $u_r = v_r = 0$ at the boundary of the disk ($r = a$).

We use the simple Euler (forward difference) approximation to approximate u_t, u_r, v_t, v_r, and central differences to approximate u_{rr}, $u_{\theta\theta}$, v_{rr}, and $v_{\theta\theta}$. Using equally spaced points along r, θ, and t we thus denote $r_i = (\Delta r)/2 + i\Delta r$, $\theta_j = j\Delta\theta$, and $t_n = n\Delta t$, where $i = 0, 1, \ldots, M$, $j = 0, 1, \ldots, N$, $\Delta r = 1/M$, and $\Delta\theta = 2\pi/N$. We start from $r = (\Delta r)/2$ in order to avoid the singularity of the Laplacian at the origin. The center of the disk is obtained by using boundary conditions such that central points are joined in pairs separated by $\theta = \pi/2$, that is,

$$U(r_{0-1}, \theta_j, t_n) = U(r_0, \theta_{j+N/2}, t_n),$$

for $j = 0, 1, \ldots, (N/2) - 1$, and

$$U(r_{0-1}, \theta_j, t_n) = U(r_0, \theta_{j-N/2}, t_n),$$

for $j = N/2, \ldots, N$.

If $U^n_{(i,j)}$ and $V^n_{(i,j)}$ denote $U(r_i, \theta_j, t_n)$ and $V(r_i, \theta_j, t_n)$, respectively, we then solve

$$U^{n+1}_{i,j} = U^n_{i,j} + \frac{D\delta\Delta t}{(\Delta r)^2}(U^n_{(i+1,j)} - 2U^n_{(i,j)} + U^n_{(i-1,j)})$$

$$+ \frac{D\delta\Delta t}{r_i(\Delta\theta)^2}(U^n_{(i,j+1)} - 2U^n_{(i,j)} + U^n_{(i,j-1)})$$

$$+ \frac{D\delta\Delta t}{r_i\Delta r}(U^n_{(i+1,j)} - U^n_{(i,j)}) + \Delta t[\alpha U^n_{(i,j)} + V^n_{(i,j)}$$

$$- \alpha r_1 U^n_{(i,j)}(V^n_{(i,j)})^2 - r_2 U^n_{(i,j)} V^n_{(i,j)}], \qquad \text{(A2a)}$$

$$V^{n+1}_{i,j} = V^n_{i,j} + \frac{\delta\Delta t}{(\Delta r)^2}(V^n_{(i+1,j)} - 2V^n_{(i,j)} + V^n_{(i-1,j)})$$

$$+ \frac{\delta\Delta t}{r_i(\Delta\theta)^2}(V^n_{(i,j+1)} - 2V^n_{(i,j)} + V^n_{(i,j-1)})$$

$$+ \frac{\delta\Delta t}{r_i\Delta r}(V^n_{(i+1,j)} - V^n_{(i,j)}) + \Delta t[\beta V^n_{(i,j)} - \alpha U^n_{(i,j)}$$

$$+ \alpha r_1 \Delta t U^n_{(i,j)}(V^n_{(i,j)})^2 + r_2 \Delta t U^n_{(i,j)} V^n_{(i,j)}], \quad \text{(A2b)}$$

with zero-flux boundary conditions

$$U^n_{M+1,j} = U^n_{M,j}, \quad U^n_{i,N+1} = U^n_{i,N},$$

$$V^n_{M+1,j} = V^n_{M,j}, \quad V^n_{i,N+1} = V^n_{i,N}.$$

As initial conditions we use random small fluctuations around the steady state $U^0_{i,j} = 0$ and $V^0_{i,j} = 0$, for all i, j.

Given the nonlinear terms in Eqs. (A2) a rigorous analysis of the stability of the difference scheme is not an easy task. In practice, however, since important sources of instability are the higher-order terms [35], necessary conditions and a good estimation of Δt are obtained by investigating the consistency and stability of Eqs. (A2) as if they were uncoupled. Thus, we consider the equations

$$u_t = D\delta\left(u_{rr} + \frac{1}{r^2}u_{\theta\theta} + \frac{1}{r}u_r\right) + \alpha u, \qquad \text{(A3a)}$$

$$v_t = \delta\left(v_{rr} + \frac{1}{r^2}v_{\theta\theta} + \frac{1}{r}v_r\right) + \beta v. \qquad \text{(A3b)}$$

As above, the finite-difference discretization of Eq. (A3a) is

$$U^{n+1}_{i,j} = U^n_{i,j} + \frac{D\delta\Delta t}{(\Delta r)^2}(U^n_{(i+1,j)} - 2U^n_{(i,j)} + U^n_{(i-1,j)})$$

$$+ \frac{D\delta\Delta t}{r_i(\Delta\theta)^2}(U^n_{(i,j+1)} - 2U^n_{(i,j)} + U^n_{(i,j-1)})$$

$$+ \frac{D\delta\Delta t}{r_i\Delta r}(U^n_{(i+1,j)} - U^n_{(i,j)}) + \alpha\Delta t U^n_{(i,j)}. \quad \text{(A4)}$$

The truncation errors arise from the Taylor series expansions used to approximate derivatives

$$\frac{U^{n+1}_{i,j} - U^n_{i,j}}{\Delta t} = u_t + \frac{\Delta t}{2}u_{tt}(\xi) \quad (t \leq \xi \leq t + \Delta t)$$

and

$$\frac{U^n_{i+1,j} - 2U^n_{i,j} + U^n_{i-1,j}}{(\Delta r)^2}$$

$$= u_{rr} + \frac{(\Delta r)^2}{12}u_{rrrr}(\xi)(r - \Delta r \leq \xi \leq r + \Delta r),$$

with similar expressions for u_r and $u_{\theta\theta}$.

From these equations, we can calculate the truncation error introduced by the finite-difference discretization of Eq. (A3a),

$$T^n_{i,j} = \frac{\Delta t}{2}u_{tt}(r_i, \theta_j, \zeta_{ijn}) + \frac{(\Delta r)^2}{12}u_{rrrr}(\nu_{ijn}, \theta_j, t_n)$$

$$+ \frac{(\Delta\theta)^2}{12}u_{\theta\theta\theta\theta}(r_i, \xi_{ijn}, t_n) + \frac{\Delta r}{2}u_{rr}(\chi_{ijn}, \theta_j, t_n),$$

which is $O(\Delta t) + O(\Delta r^2) + O(\Delta\theta^2) + O(\Delta r)$. By assuming that the involved derivatives are bounded, the truncation error goes to zero as Δt, Δr, and $\Delta\theta$ go to zero. Consequently, the numerical method is consistent with the partial differential equation (A3a).

To determine when the method is stable, we find the equation satisfied by the error $e = U - u$. By definition of the truncation error, the exact solution u satisfies

$$u^{n+1}_{i,j} = u^n_{i,j} + \frac{D\delta\Delta t}{(\Delta r)^2}(u^n_{(i+1,j)} - 2u^n_{(i,j)} + u^n_{(i-1,j)})$$

$$+ \frac{D\delta\Delta t}{r_i(\Delta\theta)^2}(u^n_{(i,j+1)} - 2u^n_{(i,j)} + u^n_{(i,j-1)})$$

$$+ \frac{D\delta\Delta t}{r_i\Delta r}(u^n_{(i+1,j)} - u^n_{(i,j)}) + \alpha\Delta t u^n_{(i,j)} + \Delta t T^n_{i,j}.$$

By substracting Eq. (A4) from this equation, after grouping common terms, we obtain

$$e_{(i,j)}^{n+1} = \left(1 - 2\frac{D\delta\Delta t}{(\Delta r)^2} - 2\frac{D\delta\Delta t}{r_i(\Delta\theta)^2} - \frac{D\delta\Delta t}{r_i\Delta r} + \alpha\Delta t\right)e_{(i,j)}^n$$

$$+ \left(\frac{D\delta\Delta t}{(\Delta r)^2} + \frac{D\delta\Delta t}{r_i\Delta r}\right)e_{(i+1,j)}^n + \left(\frac{D\delta\Delta t}{(\Delta r)^2}\right)e_{(i-1,j)}^n$$

$$+ \left(\frac{D\delta\Delta t}{r_i(\Delta\theta)^2}\right)e_{(i,j+1)}^n + \left(\frac{D\delta\Delta t}{r_i(\Delta\theta)^2}\right)e_{(i,j-1)}^n - \Delta t T_{i,j}^n.$$

$$\text{(A5)}$$

If we define $T_{\max} = \max|T_{(i,j)}^n|$ and $E^n = \max|e_{(i,j)}^n|$, for $1 \le i \le M$ and $0 \le j \le N$, from Eq. (A5) we get

$$|e_{(i,j)}^{n+1}| \le \left|1 - 2\frac{D\delta\Delta t}{(\Delta r)^2} - 2\frac{D\delta\Delta t}{r_i(\Delta\theta)^2} - \frac{D\delta\Delta t}{r_i\Delta r} + \alpha\Delta t\right|E^n$$

$$+ \left|\frac{D\delta\Delta t}{(\Delta r)^2} + \frac{D\delta\Delta t}{r_i\Delta r}\right|E^n + \left|\frac{D\delta\Delta t}{(\Delta r)^2}\right|E^n + \left|2\frac{D\delta\Delta t}{r_i(\Delta\theta)^2}\right|E^n$$

$$+ \Delta t T_{\max}. \tag{A6}$$

The absolute value sign can be removed provided that all the terms under absolute value sign are nonnegative. Since $D > 0$ and $\delta > 0$, we assume that

$$\alpha \ge 0, \tag{A7a}$$

$$1 \ge 2\frac{D\delta\Delta t}{(\Delta r)^2} + 2\frac{D\delta\Delta t}{r_i(\Delta\theta)^2} + \frac{D\delta\Delta t}{r_i\Delta r}, \tag{A7b}$$

so that, after removing absolute value signs in Eq. (A6) and simplifying, we obtain

$$|e_{(i,j)}^{n+1}| \le E^n + \alpha\Delta t E^n + \Delta t T_{\max} = (1 + \alpha\Delta t)E^n + \Delta t T_{\max}.$$

It can be proved (see, for instance, theorem 1.2.1 of Ref. [35]) that the above sequence of inequalities with nonnegative numbers is equivalent to

$$|e_{(i,j)}^n| \le e^{\alpha n\Delta t}(E^0 + n\Delta t T_{\max}) = e^{\alpha n\Delta t}n\Delta t T_{\max},$$

where we used the fact that $E^0 = 0$. Thus, as a fixed value of t_n, the error goes to zero as $T_{\max} \to 0$, and Eq. (A4) is stable under the assumptions (A7).

The above stability analysis is also valid for the discretization of Eq. (A3b), with the only difference that if $\alpha \ge 0$ [assumption (A7a)], then, according to the first condition in Eq. (3) β is negative ($\beta \le -\alpha$) [17]. Thus, the discretization of Eq. (A3b) is stable under the assumptions

$$\beta \le 0, \tag{A8a}$$

$$1 \ge 2\frac{\delta\Delta t}{(\Delta r)^2} + 2\frac{\delta\Delta t}{r_i(\Delta\theta)^2} + \frac{\delta\Delta t}{r_i\Delta r} + |\beta|\Delta t. \tag{A8b}$$

TABLE I. Normalized magnitudes of the coefficients for the Fourier-Bessel decomposition of the pattern in Fig. 4(c).

m/n	1	2	3	4	5	6	7
0	0.372	0.021	1.000	0.058	0.013	0.004	0.015
1	0.003	0.006	0.012	0.004	0.002	0.001	0.000
2	0.002	0.016	0.004	0.003	0.002	0.002	0.001
3	0.002	0.010	0.002	0.003	0.002	0.002	0.002
4	0.002	0.010	0.000	0.002	0.002	0.002	0.002
5	0.594	0.057	0.012	0.017	0.014	0.011	0.011
6	0.002	0.008	0.003	0.000	0.000	0.001	0.001
7	0.002	0.007	0.003	0.000	0.000	0.001	0.001

Equations (A7b) and (A8b) can be written in a more transparent way if we take into account that, since we are avoiding the origin $r = 0$, $\min(r_i) = r_0 = (\Delta r/2)$. By substituting this into Eqs. (A7b) and (A8b) and rearranging the terms we obtain

$$\Delta t \le \frac{1}{\dfrac{4D\delta}{(\Delta r)^2} + \dfrac{4D\delta}{\Delta r(\Delta\theta)^2}}, \tag{A9a}$$

$$\Delta t \le \frac{1}{\dfrac{4\delta}{(\Delta r)^2} + \dfrac{4\delta}{\Delta r(\Delta\theta)^2} + |\beta|}, \tag{A9b}$$

respectively. Both inequalities provide necessary conditions for the stability of Eq. (A2).

The values used in all our calculations are $D = 0.516$, $\Delta r = 1/34$, $\Delta\theta = 2\pi/68$, and $\beta = -0.91$. Thus by considering, for example, the value of δ to obtain the pentagonal
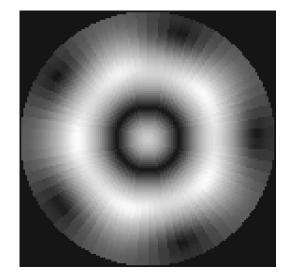

FIG. 10. Reconstructed image using the complex coefficients tabulated in Table I and Eq. (B1).

pattern in Fig. 2(a) ($\delta = 0.01\,011$) we get $\Delta t \leq 0.009\,326$ and $\Delta t \leq 0.004\,791$, respectively.

APPENDIX B: MODAL DECOMPOSITION

The principal modes involved in the Turing patterns simulated in this work can be revealed by means of a modal decomposition. In particular, the solution of Eqs. (1), $u(r,\theta)$, can be expanded in a Fourier-Bessel series as

$$u(r,\theta) = \sum_{m=0}^{\infty} \sum_{n=1}^{\infty} C_{mn} J_m(k_{mn}r) e^{im\theta}, \qquad \text{(B1)}$$

where $k_{mn} = \kappa_{mn}/a$, as defined in Sec. II.

Using the orthonormality and completeness of $J_m(k_{mn}r)e^{im\theta}$, the complex coefficients C_{mn} are given by

$$C_{mn} = \frac{k_{mn}^2}{\pi[(k_{mn}a)^2 - m^2][J_m(k_{mn}a)]^2}$$

$$\times \int_0^a \int_0^{2\pi} u(r,\theta) r J_m(k_{mn}r) e^{-im\theta} \, d\theta \, dr.$$

By examining the magnitude $|C_{mn}|$ of these coefficients, we can determine the principal modes of the function $u(r,\theta)$.

We performed the Fourier-Bessel decomposition of the pattern in Fig. 4(c). In Table I, the normalized magnitudes $|C_{mn}|$ for $m = 0,1,\ldots,7$ and $n = 1,2,\ldots,7$, are tabulated. It can be seen that the more relevant modes are (03), (51), and (01). Since J_0 is nonzero at the origin, the enhancement of modes k_{03} and k_{01} account for the central spot in the pentagonal pattern.

In order to verify our result, we use the obtained (complex) coefficients, to reconstruct the pattern using Eq. (B1). The result is shown in Fig. 10.

[1] F.H.C. Hotchkiss, Paleobiology **24**, 200 (1998), and references therein.

[2] D. Gil, P. Domínguez, M. Torres, and I. Jiménez, Geobios **32**, 861 (1999), and references therein.

[3] A.J. Koch and H. Meinhardt, Rev. Mod. Phys. **66**, 1481 (1994).

[4] J. Boissonade, E. Dulos, and P. De Kepper, in *Chemical Waves and Patterns*, edited by R. Kapral and K. Showalter (Kluwer, Dordrecht, The Netherlands, 1995), p. 221.

[5] P. Borckmans, G. Dewel, A. Dewit, and D. Walgraef, in *Chemical Waves and Patterns* (Ref. [4]), p. 323.

[6] D.J. Wollkind and L.E. Stephenson, in *Mathematical Models for Biological Pattern Formation*, edited by P. K. Maini and H.G. Othmer (Springer-Verlag, New York, 2000), p. 113.

[7] R.B. Emlet, Biol. Bull. **174**, 4 (1988).

[8] P.K. Maini, M.R. Myerscough, K.H. Winters and J.D. Murray, Bull. Math. Biol. **53**, 701 (1991).

[9] A.M. Turing, Philos. Trans. R. Soc. London, Ser. B Biol. Sci. **237**, 37 (1952).

[10] J.D. Murray, *Mathematical Biology*, 2nd ed. (Springer-Verlag, New York, 1993).

[11] H. Meinhardt, *Models of Biological Pattern Formation* (Academic Press, London, 1982).

[12] J.D. Murray, Philos. Trans. R. Soc. London, Ser. B Biol. Sci. **295**, 473 (1981); J. Theor. Biol. **88**, 161 (1981).

[13] H. Meinhardt and M. Klinger, J. Theor. Biol. **126**, 63 (1987); H. Meinhardt, *The Algorithmic Beauty of Sea Shells*, 2nd ed. (Springer, New York, 1998).

[14] S. Kondo and R. Asai, Nature (London) **376**, 765 (1995).

[15] T. Hofer and P.K. Maini, Nature (London) **380**, 678 (1996).

[16] C. Varea, J.L. Aragón, and R.A. Barrio, Phys. Rev. E **56**, 1250 (1997).

[17] R.A. Barrio, C. Varea, J.L. Aragón, and P.K. Maini, Bull. Math. Biol. **61**, 483 (1999).

[18] K.J. Painter, P.K. Maini, and H.G. Othmer, Proc. Natl. Acad. Sci. U.S.A. **96**, 5549 (1999).

[19] C. Varea, J.L. Aragón, and R.A. Barrio, Phys. Rev. E **60**, 4588 (1999).

[20] S.S. Liaw, C.C. Yang, R.T. Liu, and J.T. Hong, Phys. Rev. E **64**, 041909 (2001).

[21] Y. Chen and A.F. Schler, Nature (London) **411**, 607 (2001).

[22] R. Dillon, P.K. Maini, and H.G. Othmer, J. Math. Biol. **32**, 345 (1994).

[23] E.J. Crampin, E.A. Gaffney, and P.K. Maini, Bull. Math. Biol. **61**, 1093 (1999).

[24] C.J. Lowe and G.A. Wray, Nature (London) **389**, 718 (1997).

[25] G. Panganiban *et al.*, Proc. Natl. Acad. Sci. U.S.A. **94**, 5162 (1997).

[26] A clear example of the disklike arrangement of the five primary podia is also shown in Fig. 212 of L.H. Hyman, *The Invertebrates, Echinodermata* (McGraw-Hill, New York, 1995), Vol. IV, p. 497.

[27] B. David and R. Mooi, in *Echinoderms: San Francisco*, edited by R. Mooi and M. Telford (Balkema, Rotterdam, 1998), p. 21.

[28] H. Meinhardt, Dev. Biol. **157**, 321 (1993).

[29] B.N. Nagorcka, Austral. J. Agric. Res. **46**, 333 (1995).

[30] H.F. Nijhout, Proc. R. Soc. London, Ser. B **239**, 81 (1990).

[31] H. Hess, W. I. Ausich, C.E. Brett, and M. Simms, *Fossil Crinoids* (Cambridge University Press, Cambridge, UK, 1999).

[32] G. Ubaghs, in *Treatise on Invertebrate Paleontology. Part T: Echinodermata 2*, edited by R.C. Moore and C. Teichert (The Geological Society of America/The University of Kansas, Boulder, CO/Lawrence, KS, 1978), Vol. 2.

[33] R.D.K. Thomas, R.M. Shearman, and G.W. Stewart, Science **288**, 1239 (2000).

[34] The appearance and role of Dirichlet domains in biology is discussed in the A.J. Koch and H. Meinhardt review paper [3] in the context of the giraffe coat pattern.

[35] G. Sewell, *The Numerical Solution of Ordinary and Partial Differential Equations* (Academic Press, London, 1988).